IX International Conference on Particle-Based Methods
PARTICLES 2025
J. Bonet, M. Cremonesi, A. Franci, A. Gil (Eds)

SIMULATING TURBULENT FLOWS WITH SYNTHETIC INFLOW TURBULENCE USING SMOOTHED PARTICLE HYDRODYNAMICS

MARCO GOEBEL [*, †], NIKLAS BUERKLE [†], GEOFFROY CHAUSSONNET [†], RAINER KOCH [†] AND HANS-JOERG BAUER [†]

[†] Institute of Thermal Turbomachinery (ITS)
Karlsruhe Institute of Technology (KIT)
Straße am Forum 6, 76131 Karlsruhe, Germany
email: marco.goebel@kit.edu

Key words: SPH, Turbulence Modelling, Boundary Condition, Turbulent Inflow

Abstract. In this work, two algorithms for synthetic turbulent inflow generation are implemented within a modern transport-velocity SPH framework. Both methods are tested using three-dimensional simulations of convected isotropic turbulence with prescribed turbulence characteristics, including length scale, time scale and fluctuation intensity. The capability to model anisotropic turbulence is further assessed by simulating turbulent flow in a circular pipe. Near the turbulent inlet, a high agreement with the prescribed statistics is achieved. Coherent structures are successfully formed and exhibit realistic downstream evolution, demonstrating promising potential for future applications to more complex scenarios, such as shear-driven liquid atomization.

1 INTRODUCTION

The accurate modelling of turbulent flows is still one of the key challenges for the industrial application of Smoothed Particle Hydrodynamics (SPH) [1]. In recent studies, Antuono and Okraschevski independently concluded that Smoothed Particle Hydrodynamics (SPH) can be embedded within the framework of Large Eddy Simulation (LES) [2,3]. However, the focus of their studies was mainly on generic flow configurations to show SPH's basic ability to predict the characteristics of turbulent flows like the cascade of turbulent kinetic energy (TKE), as well as the impact of different approaches to sub-filter-stress (SFS) modelling.

It is well established that many complex flow configurations cannot be accurately represented using periodic or closed domains and therefore require the use of permeable boundary conditions. However, for LES-type simulations, prescribing only the mean flow at these boundaries is often insufficient. For canonical flows such as free jets, mixing layers, or jet in cross-flow configurations, upstream turbulence critically governs entrainment, mixing efficiency and the development of large-scale structures. In two-phase flows, turbulent dynamics also drive interfacial instabilities, strongly influencing liquid atomization and wave formation [4,5]. While turbulent fluctuations at the inlet boundaries may be neglected if they are placed sufficiently far from the region of interest, this approach is computationally expensive, as it requires extending the domain to capture the entire turbulence development region. This is particularly relevant for SPH simulations, which typically employ a uniform

spatial resolution due to the ongoing challenge of developing high-fidelity schemes for spatial adaptivity [1]. Therefore, to accurately model turbulent flows, it is desirable to be able to prescribe both the mean velocity profiles as well as the associated turbulent fluctuations at permeable boundaries.

Due to these considerations, a range of algorithms has been proposed to impose synthetic fluctuations that mimic realistic coherent structures for grid-based methods. So far, the integration of such methods in SPH simulations has remained largely unexplored.

Therefore, the objective of this work is to investigate the applicability of existing synthetic inflow generation techniques within modern SPH schemes.

2 NUMERICAL METHOD

The following section provides a brief overview of the employed SPH scheme as well as the implementation of the methods for generating turbulent inflow.

2.1 Smoothed Particle Hydrodynamics

In this work, a modern, weakly compressible transport velocity scheme is used. Particles are advected with a transport velocity $\vec{u} + \delta\vec{u}$ consisting of the Lagrangian velocity $\vec{u}$ and the shift-velocity $\delta\vec{u}$, which is calculated according to Lind [6]. Time integration is conducted using a modified Velocity-Verlet scheme [7]. The temporal derivatives of the density ρ and velocity $\vec{u}$ of a particle i are derived as

$$\frac{\mathrm{d}\rho_i}{\mathrm{d}t} = -\rho_i \sum_j V_j \left(\vec{u}_j - \vec{u}_i\right) \cdot \vec{\nabla} W_{ij} + \delta h D_i^{\rho} + \delta\vec{u}_i \cdot \sum_j V_j \left(\rho_j - \rho_i\right) \vec{\nabla} W_{ij} \tag{1}$$

$$\frac{\mathrm{d}\vec{u}_i}{\mathrm{d}t} = \vec{a}_{p,i} + \vec{a}_{\mathrm{visc},i} + \delta\vec{u}_i \cdot \sum_j V_j \left(\vec{u}_j - \vec{u}_i\right) \otimes \vec{\nabla} W_{ij}. \tag{2}$$

The mass of each particle m is kept constant within the domain, and the particle volume V is calculated as $V = m/\rho$. The final term on the right-hand side of equations 1 and 2 corresponds to the corrections due to shifting for continuity and momentum. The density diffusion term D_i^{ρ} is evaluated according to Antuono [8] and is scaled by the smoothing length h and the constant $\delta = 0.1$. To avoid tensile instabilities, the acceleration due to the pressure gradient $\vec{a}_p$ is computed using the formulation of Sun [9]. Viscous forces $\vec{a}_{\mathrm{visc}}$ are modelled according to Szewc [10]. By modifying the viscosity term near solid walls, a no-slip condition is imposed [11]. In SPH-LES, viscous forces are commonly complemented by an explicit SFS term. However, as demonstrated by Okraschevski [3, 12], explicit SFS models tend to introduce excessive numerical dissipation in the inertial sub-range, leading to a substantial deterioration of results. Consistent with these findings, in an initial pre-study of the 3D Taylor–Green vortex at $Re = 10000$ using the present scheme, the best agreement with DNS reference data was obtained when the contribution of a SFS model was neglected. Consequently, no explicit SFS model is employed in the present work. Finally, the system of equations is closed using the barotropic Tait equation,

$$p = \frac{\rho_0 {c_0}^2}{\gamma} \left[\left(\frac{\rho}{\rho_0} \right)^{\gamma} - 1 \right]. \tag{3}$$

The artificial speed of sound c_0 is set such that $Ma = u/c_0 < 0.1$. For the simulations presented, a reference density $\rho_0 = 1$ and an isentropic exponent $\gamma = 1$ are assumed.

2.2 Inflow Methods

The following two methods to impose turbulent fluctuations at inlet boundaries have been implemented in the previously presented SPH scheme:

(i) the Random Flow Generator (RFG), originally proposed by Kraichnan [13, 14]

(ii) the Digital Filter (DF) method of Klein [5].

Both methods offer distinct advantages and drawbacks. The RFG has the crucial benefit of producing a divergence-free inflow field; however, it can only reproduce the correct autocorrelation between turbulent fluctuations for a limited range of scales and discrete modes. In contrast, the DF facilitates the prescription of fluctuations continuous across all scales using a predefined correlation function but does not inherently guarantee a divergence-free inflow field.

2.2.1 Random Flow Generator

The RFG builds a divergence-free turbulent inflow field through the superposition of N randomly sampled harmonic Fourier modes. The implemented procedure consists of the following steps:

(i) Given an anisotropic Reynolds-stress tensor $R_{ij} = \overline{u_i' u_j'}$, an orthogonal transformation tensor A_{ij} is found that diagonalizes R_{ij}:

$$A_{mi}\, R_{ij}\, A_{nj} = \Lambda_{mn}, \qquad \Lambda_{mn} = \begin{cases} \lambda_m^2, & m = n, \\ 0, & m \neq n. \end{cases} \tag{4}$$

The diagonal elements λ_m are the velocity fluctuations u_i' along the transformed axes. The matrix A_{ij} contains the corresponding eigenvectors of R_{ij}.

(ii) Generate a transient flow field by the superposition of harmonic modes

$$v_i(\vec{x}, t) = \sqrt{\frac{2}{N}} \sum_{n=1}^{N} \left[p_i^n \cos\left(\tilde{k}_j^n \tilde{x}_j + \omega_n \tilde{t}\right) + q_i^n \sin\left(\tilde{k}_j^n \tilde{x}_j + \omega_n \tilde{t}\right) \right], \tag{5}$$

$$\tilde{x}_j = \frac{x_j}{L_{\text{turb}}}, \quad \tilde{t} = \frac{t}{\tau_{\text{turb}}}, \quad \tilde{k}_j^n = k_j^n \frac{|\vec{\lambda}|}{\lambda_j}. \tag{6}$$

The prescribed turbulent length- and timescale are denoted by L_{turb} and τ_{turb} respectively. The specific wavenumber vector $\tilde{k}_j^n$ is scaled with the inverse norm of the respective eigenwert to resemble the effects of anisotropy. To satisfy the divergence-free condition, the amplitude vectors $\vec{p}_i^n$ and $\vec{q}_i^n$ are constructed by the vector product,

$$p_i^n = \varepsilon_{ijm} \zeta_j^n k_m^n, \quad q_i^n = \varepsilon_{ijm} \xi_j^n k_m^n, \quad \text{using} \tag{7}$$

$$\zeta_i^n, \xi_i^n, \omega_n \in N(0,1), \quad k_i^n \in N(0, 1/2). \tag{8}$$

This ensures zero divergence for isotropic turbulence and nearly zero divergence for anisotropic turbulence. The N-random vectors $\vec{\zeta}$, $\vec{\xi}$ and $\vec{k}$ as well as the random frequencies ω are sampled from a normal distribution $N(\mu, \sigma)$ with mean μ and standard deviation σ, respectively.

(iii) Project the flow field $\vec{v}$ back into original space using the expression

$$u_i'(\vec{x},t) = \mathrm{A_{ik}}\,\lambda_\mathrm{i}\,v_i(\vec{x},t). \tag{9}$$

The sampling of random variables and the orthogonal transformation is conducted once on simulation initialization, where results are saved as arrays to avoid continuous recomputation. During this work, 250 discrete modes are used for building the inlet flow fields. During the simulation, only steps (ii) and (iii) are repeated. The computational overhead and memory consumption of this method can be considered to be low.

2.2.2 Digital Filter Method

For the implementation of the Digital Filter method [5], fluctuations are computed for a separate two-dimensional grid that requires uniform spacing. The grid dimensions (M_y, M_z) denote the number of points in the y- and z-directions, where the y–z plane corresponds to the inlet cross-section. After fluctuations are computed for each grid point, the field of fluctuations is mapped to the inflow plane via interpolation. The core algorithm is outlined below, for details please refer to Klein et al. [5]:

(i) Choose a filter scale $L_y = n_y \Delta y$ and $L_z = n_z \Delta z$ corresponding to the turbulent length scale as well as $L_x = n_x \Delta x$ which corresponds by Taylor's hypothesis to the turbulent timescale.

(ii) Initialize three random buffers B of dimension $\left[-N_x : N_x, -N_y + 1 : M_y + N_y, -N_z + 1 : M_z + N_z\right]$, where $M_y \times M_z$ corresponds to the grid dimension and $N_i \geq 2n_i, i = x, y, z$.

(iii) Compute the filter coefficients b based on the predefined auto-correlation function.

(iv) Compute the fluctuations by the following filter operation for $j = 1, .., M_y, k = 1, .., M_z$

$$u_i'(j,k) = \sum_{i'=-N_x}^{N_x} \sum_{j'=-N_y}^{N_y} \sum_{k'=-N_z}^{N_z} b(i',j',k') B(i', j+j', k+k') \,. \tag{10}$$

(v) Scale the fluctuations to match the prescribed Reynolds-stresses and map them to the corresponding position on the inlet plane.

(vi) Shift the random buffers in x-direction and refill the first row with new random samples. Steps (iv) - (vi) are repeated for each update of the inflow field. Due to the much higher numerical overhead of this method as well as the small time step width dt in weakly-compressible SPH simulations, the inflow field is updated only every nth timestep, such that the condition $\tau_\mathrm{turb}/(dt \times n) \approx 0.02$ is met. Furthermore, the grid that is used for the computation of fluctuations has only half the spatial resolution of the SPH discretization.

2.3 Implementation at SPH Boundaries

The previous sections outlined the core SPH-scheme and described the methods used to generate transient inlet flow fields $\vec{u}(\vec{x},t)$ with prescribed temporal and spatial correlations. However, the main question that motivates this work is whether these fluctuations can be successfully imposed on the inlet flow field of SPH simulations.

For the current implementation, a buffer-particle approach is used [15]. Therefore, at the location of the permeable boundary, marker particles are created. In the direction of the normal vector pointing outside the SPH domain, buffer particles are added. This ensures full kernel support for regular particles inside the SPH domain. Buffer particles are advected with a constant velocity imposed by the corresponding marker and thus enforcing a Dirichlet-type boundary. At the outer layer of the buffer, new particles are generated. In this work, the

approach has been adapted to handle a temporally and spatially varying inflow velocity field $\vec{u}(\vec{x},t)$, such that

$$\vec{u}(\vec{x},t) = \overrightarrow{\overline{u}}(\vec{x}) + \vec{u}'(\vec{x},t). \tag{11}$$

For each marker, its mean-velocity vector as well as Reynolds-stress components are stored in a pre-processing step. Based on these, as well as the provided length- and time scales, the inflow field $\vec{u}(\vec{x},t)$ is calculated. The core procedure is depicted in Figure 1. Fluctuations are computed either for the marker particles with position $\vec{x}_{\mathrm{m}}$ and then applied to their corresponding buffer particles (Fig. 1a) or directly computed for each buffer particle with position $\vec{x}_{\mathrm{b},i}$ (Fig. 1b). The second approach has the advantage of including positional information in the marker-plane's normal direction. For the RFG method, which generates a three-dimensional, divergence-free inflow field, this is advantageous due to the resulting non-zero contribution in the normal direction to the divergence operator. On the other hand, depending on the radius of the employed kernel, the number of buffer particles is typically at least three times larger than the number of marker particles, leading to higher numerical overhead. Regarding the DF implementation, this option is not recommended due to its much higher numerical cost as well as the generated field being inherently not divergence-free.

Regarding the buffer particles, continuously advecting them with their instantaneous velocities causes a highly disturbed particle order due to the stochastic nature of fluctuations. Therefore, to maintain a regular particle order inside the buffer zone, particles are advected using their mean velocities $\overrightarrow{\overline{u}}$ instead. This modification can be interpreted as shifting the buffer particles inversely to the contribution of fluctuations $\vec{u}'$. Thus, the shift velocity $\delta\vec{u} = -\vec{u}'$ can be added as an additional variable to each buffer particle, which can then be taken into account by the regular SPH particles using a modified correction term in equations 1 and 2 for continuity and momentum, e.g. using the formulation of Sun [16]. To keep the discussion of results concise and avoid introducing additional parameters, this option is disabled for the simulations presented. Since we only consider moderate turbulence intensities in this study, we consider $u' \ll \overline{u}$. Thus, the shifting-velocities and therefore the influence of the modified shifting corrections observed so far is minor; however, more in-depth investigations are still ongoing.

Pressure and density of the marker particles are interpolated from their neighboring regular particles using Shepard interpolation, which are then projected toward their respective buffer

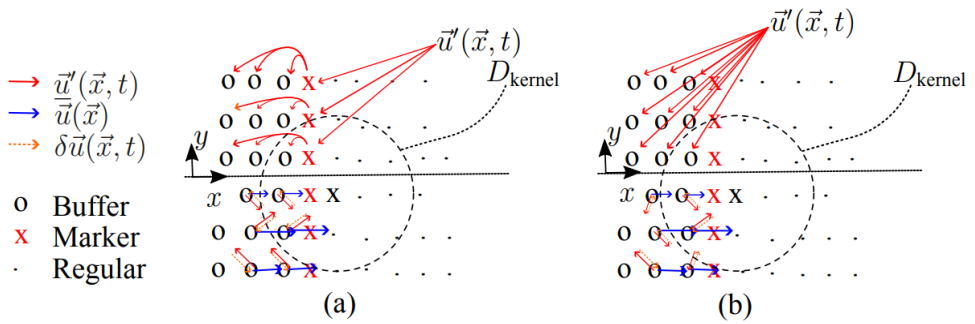

Figure 1: Implementation of the synthetic fluctuations at the SPH-boundary. Top part shows the distribution of fluctuations, bottom part the interplay of advection velocity $\vec{u}$, fluctuation $\vec{u}'$ and shift-velocity $\delta\vec{u}$. (a) Fluctuations applied to markers and then mapped to corresponding buffer particles, (b) Fluctuations directly applied to buffer particles.

particles. This weakly enforces a zero-gradient condition for pressure and density.

Furthermore, it was observed that even small deviations in the spatially averaged instantaneous velocity of the inflow plane on the order of 0.1 % induce significant fluctuations in density and pressure. This is because the inflow method generates inherently unsteady velocity fields, and the prescribed mean velocity is conserved only statistically, when averaged over sufficiently long sampling intervals. To counteract these spurious fluctuations, the inlet mass flow is adjusted for each timestep by applying a correction factor that scales the velocity component normal to the boundary, thereby enforcing the prescribed mass flow rate. It should be noted, however, that this procedure may lead to slight overshoots in the boundary-normal velocity fluctuations.

3 TESTCASES

In the following section, the implementations will be tested for two cases of increasing levels of complexity, starting out with the decay of convected isotropic turbulence. This serves as a valuable setup to analyze fundamental aspects of the implementations. Finally, turbulent pipe flow at $Re_\tau = 495$ is also examined to study a case involving complex anisotropic turbulence.

3.1 Convected isotropic Turbulence

As a first test case, the decay of convected isotropic turbulence in the streamwise direction is considered, using a domain that is periodic in the lateral directions. This setup is conceptually comparable to the decay of grid-generated turbulence, a configuration that has been widely studied in experiments.

The domain has a square cross-section with $b = 2H$ and length $L = 10H$, with $H = 1$ m. At the inlet, a mean velocity of $U_{\text{Bulk}} = 1\ \text{m/s}$ is imposed, as well as a turbulence intensity of 5 %, representing a realistic ratio of u'/U_{Bulk} typically observed in developed channel and pipe flows. The prescribed turbulence is assumed to be isotropic. Simulations are performed with turbulent length scales $\mathcal{L} = 0.6H$ and $\mathcal{L} = H$ as well as a kinematic viscosity of $\nu = 10^{-4}\ \text{m}^2\,\text{s}^{-1}$. This corresponds to Reynolds numbers of $Re_{\mathcal{L}} = u'_{\text{mag}}\mathcal{L}/\nu = 500$ and 860, respectively, both representative of overall weak turbulence. To extend the study toward higher turbulence levels, additional simulations are conducted for $\mathcal{L} = H$ with kinematic viscosities of $\nu = 10^{-5}\ \text{m}^2\,\text{s}^{-1}$and $\nu = 10^{-6}\ \text{m}^2\,\text{s}^{-1}$, resulting in $Re_{\mathcal{L}} = 8.6 \times 10^3$ and $Re_{\mathcal{L}} = 8.6 \times 10^4$. The spatial resolution is set to $\Delta x = 0.02$ m, resulting in 5×10^6 particles. A quintic B-spline kernel with kernel radius $R_k = 3dx$ is used for all simulations. The turbulent time scale is linked to its length scale via $\tau_{\text{turb}} = \mathcal{L}/U_{\text{bulk}}$. A minimum of 15 flow-through times tU_{Bulk}/L were simulated, with the final 10 used for extracting turbulence statistics, which were sampled every 10^{th} timestep. To this end, a sampling procedure was developed where fluctuations were evaluated on lateral planes populated with evenly spaced marker particles. Flow quantities were interpolated to these planes using Shepard interpolation, and statistics were accumulated over time. While Shepard interpolation proved sufficient for statistical sampling, the accurate computation of turbulent energy spectra required higher-order interpolation, like 2^{nd} order Moving-Least-Squares (MLS) [17], which was applied at selected probe points.

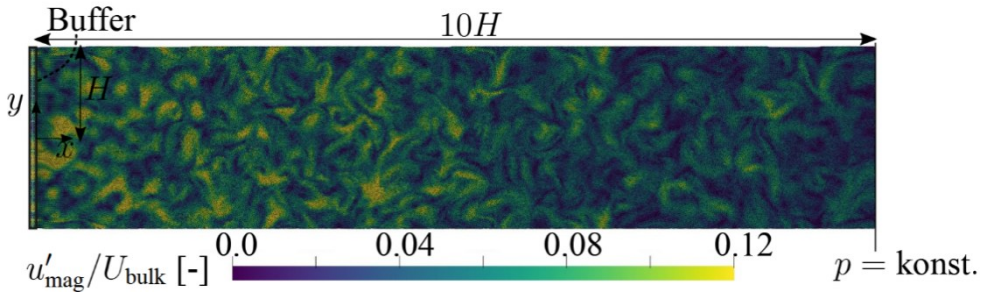

Figure 2: Instantaneous fluctuation magnitude u'_{mag} at $tU_{Bulk}/L = 8$ using the RFG with $\mathcal{L} = 0.6H$.

3.1.1 Results

To illustrate the quantitative development of the turbulent flow field, the contour of the normalized instantaneous velocity fluctuation magnitude is depicted in Figure 2. It can be observed that the inlet fluctuations lead to coherent turbulent structures. In the immediate vicinity of the inlet, predominantly large-scale structures are found, while further downstream, these evolve into finer, delicate structures. This transition is further highlighted by the iso-surface of Q-criterion presented in Figure 3, which visualizes the intricate vortical structures emerging within the flow.

The quantitative evolution of turbulence intensity is depicted in Fig. 4a for the DF and the RFG implementations. Values are averaged for the respective lateral planes. All three simulations were conducted for the low Reynolds number case, with a length scale $\mathcal{L} = 0.6H$. Under the assumption of Taylor's hypothesis, the decay of HIT can be approximately described by the power-law $k(x) = k_0(x - x_0)^{-n}$, with $n \approx 1.2$ [18]. The exact fitting of this power-law is not trivial and out of the scope of this work. A basic fit was obtained for each simulation, using data collected downstream of $x/H = 2$ as input, which is further depicted for all cases. The simulation results are largely consistent, with the main difference being a slight underestimation of turbulence intensity when using the buffer-implementation of the RFG. Overall, the deviation from the prescribed turbulence intensity remains below 10 %. As shown in Fig. 4b, which depicts a variation of Reynolds number by modifying length scale as well as kinematic viscosity, such an underestimation occurs exclusively at the smaller length scale. The most pronounced deviation between the DF method and RFG is observed in the near-field region of the inlet ($x/H < 2$). While the extrapolated rate of decay is reproduced by the DF

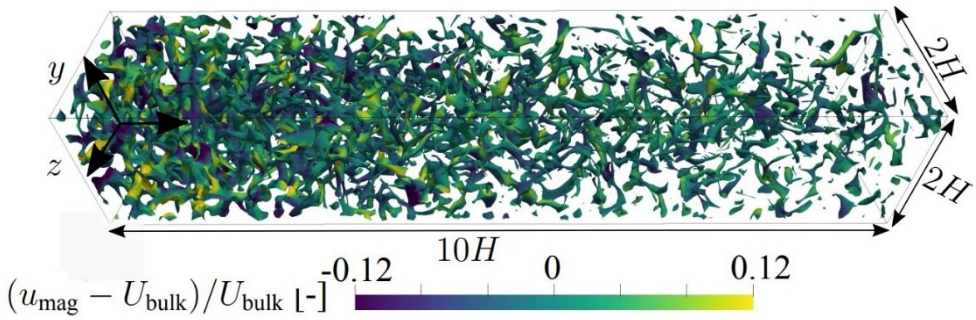

Figure 3: Iso-surface of Q-Criterion at $tU_{Bulk}/L = 8$ using the RFG and $\mathcal{L} = 0.6H$.

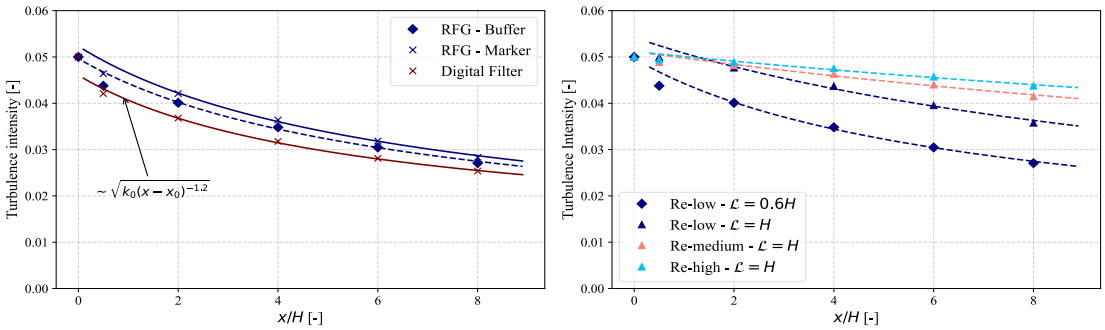

Figure 4: Decay of turbulence intensity for (a) length scale $\mathcal{L} = 0.6H$ and different inflow methods and (b) RFG buffer implementation with varying $Re_{\mathcal{L}}$.

method down to $x/H = 0.5$, a reduced decay rate is obtained with the RFG method for this region. This behavior suggests that the inflow perturbations introduced by the RFG require additional downstream distance to establish a self-similar state. The effect of reducing kinematic viscosity and thus increasing Reynolds number is depicted in Fig. 4b. The expected decrease in dissipation at higher Reynolds numbers is successfully reproduced for all simulations. Importantly, none of the simulations exhibit numerical instabilities or signs of energy accumulation at the cut-off range, despite the absence of a SFS model.

The rationale for focusing on the buffer implementation of the RFG becomes evident from the time series of normalized pressure sampled at probes at $x/H = 0.5$ and $x/H = 8$, as shown in Figure 5a and b, respectively. Due to its non-divergence-free formulation, pressure fluctuations with amplitudes significantly exceeding those expected from incompressible turbulence ($p' \approx \rho \overline{u'_{x=0} u'_{x=0}}$) emerge from the use of the DF method. Even for the case with the highest viscosity examined here, these fluctuations are only slowly damped and remain observable near the outlet. Both implementations of the RFG demonstrate improved behavior regarding pressure oscillations, indicating the importance of employing a divergence-free inflow condition. Furthermore, it is observed that applying fluctuations directly to the buffer particles leads to a reduction in pressure oscillations.

Finally, the one-dimensional spectra of TKE are presented for the high Reynolds number

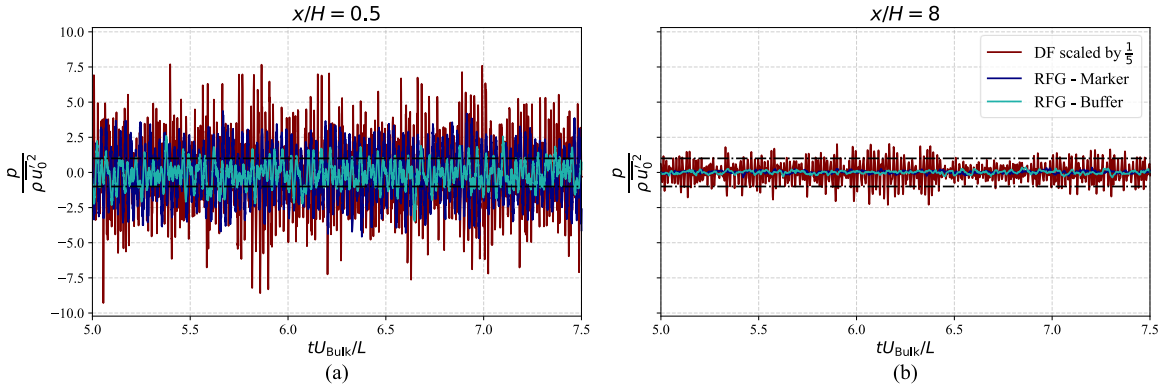

Figure 5: Time series of pressure fluctuations for $Re_{\mathcal{L}} = 500$ at (a) $x/H = 0.5$ and (b) $x/H = 8$.

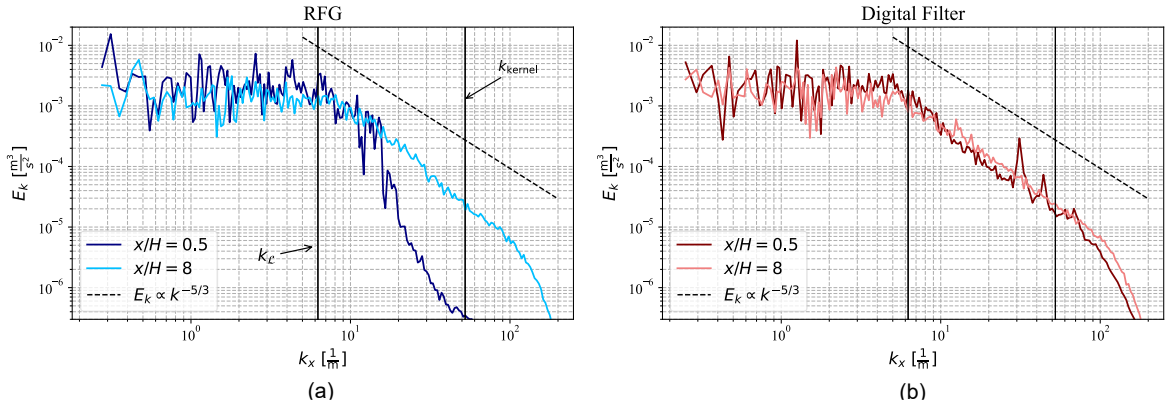

Figure 6: One-dimensional turbulent energy spectra obtained using (a) RFG and (b) Digital Filter Method.

case for both the RFG and DF method in Figure 6 comparing the near-inlet region, where the spectra are still primarily influenced by the inflow fluctuations, with the near-outlet region, where turbulence has evolved toward a more developed state. The spectra were computed from time-resolved data obtained at probes located at the center of the respective cross-section, where flow variables were interpolated using second-order MLS. Then, Taylor's hypothesis was used to relate the obtained frequencies to their corresponding spatial wavelengths k_x. As already suggested in the discussion of TKE decay, the low-energetic high wavenumber modes in Fig. 6a confirm that small-scale turbulence is underdeveloped near the inlet when using the RFG. The expected $k^{-5/3}$ scaling in the inertial sub-range is observed only in the vicinity of the prescribed length scale. In contrast, the simulation employing the DF method is shown to reproduce the prescribed autocorrelation for all modes $k < k_{\mathcal{L}}$, thereby leading to a developed inertial sub-range in the SPH simulation. Some spurious intermediate peaks are apparent in the spectra of the DF implementation, which may result from a recoupling of pressure waves with turbulence. Despite the initially imposed turbulence by the RFG lacking energy in high wave-modes, both approaches yield very similar spectra near the outlet, demonstrating the capability of the SPH scheme to recover the expected scaling in the inertial sub-range.

Based on the investigations conducted so far, the buffer RFG implementation is identified as the preferable choice, owing to its favorable behavior with respect to pressure fluctuations. In contrast, the DF method would require additional modifications, such as a divergence-free projection, in order to address this issue effectively.

3.2 Turbulent Pipe Flow

The previous case of decaying isotropic turbulence represents a highly idealized scenario compared to realistic applications of inflow turbulence. To study a more complex case, the method is applied to the turbulent flow inside a circular pipe, where both the full, strongly anisotropic Reynolds-stress tensor and the corresponding mean velocity profiles from a DNS [19] are prescribed at the inflow plane. This allows for a rigorous assessment of the method's ability to impose complex, anisotropic turbulence and to capture its subsequent development in the streamwise direction.

The studied pipe has a length of $20R$, where $R = 1$ m corresponds to the pipe radius. It is discretized using a uniform resolution with mean particle spacing dx= 0.02 m. This leads to a

total of about 10^7 particles. A moderately turbulent case with $Re_\tau = 495$ is chosen. To match the corresponding bulk Reynolds number $Re_D = 17000$, with a fixed bulk velocity $U_{\text{bulk}} = 1\ \text{m/s}$, the kinematic viscosity is set to $\nu = 1.2 \times 10^{-4}\ \text{m}^2\,\text{s}^{-1}$. For the simulation presented, the buffer RFG implementation with $\mathcal{L} = 0.6R$ was chosen. Statistical quantities were averaged over 8 flow-through times.

Some deviations to the reference DNS simulation are expected due to the coarse resolution in proximity to the wall with $y_1^+ \approx 10$, as $y_1^+ \approx 1$ would necessitate about 5×10^9 particles. The resulting Reynolds-stresses, normalized with the friction velocity $u_{\tau,\text{DNS}}$ and averaged in the circumferential direction ϕ, are presented in Fig. 7. Immediately downstream of the inlet at $x/R = 0.5$, the prescribed Reynolds-stresses are reproduced with excellent agreement, with only a slight underestimation observed near the wall. The cross-correlation $\overline{u_x' u_r'}$ is already moderately developed. Comparison of profiles near the inlet with those at $x/R = 15$ (Fig. 7b) indicates minor changes in the Reynolds-stresses, with streamwise fluctuations slightly increased and spanwise and wall-normal fluctuations dampened near the wall. Excellent agreement with the reference data is retained for $r/R < 0.5$, where the flow is highly resolved.

The development of the turbulent flow field is further illustrated in Fig. 8, which presents instantaneous snapshots of the normalized axial velocity in the centerline plane and in two cross-sectional planes. These snapshots reveal realistic coherent structures, with larger ones in the center of the pipe and finer, anisotropic structures in the near-wall region.

Another aspect that should be discussed is that the flow field produced by the RFG approach is no longer completely divergence-free for the anisotropic turbulence investigated here, causing some oscillations of pressure in the magnitude of $p^+ = p/(\rho u_\tau^2) \approx 2\text{-}10$. However, no major influence of these spurious fluctuations could be observed.

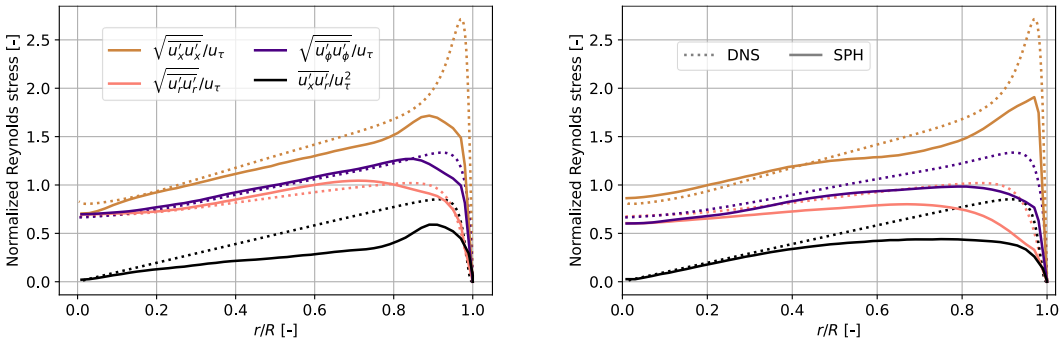

Figure 7: Normalized Reynolds-stresses obtained from SPH using the RFG compared to reference DNS solution at (a) $x/R = 0.5$ and (b) $x/R = 15$.

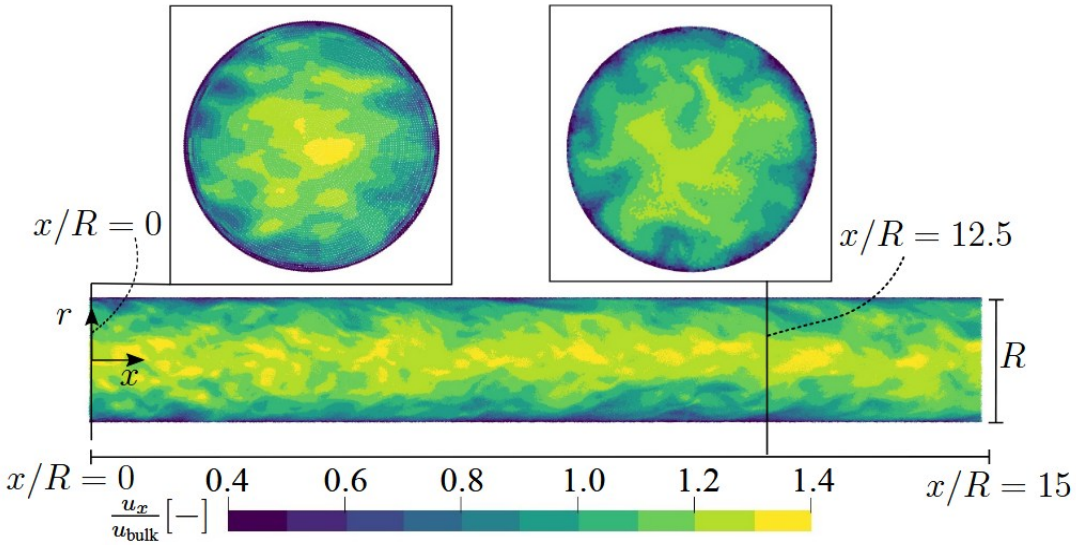

Figure 8: Instantaneous fields of axial velocity for different cross-sections.

4 CONCLUSION

Two methods for turbulent inflow generation, the Random Flow Generator (RFG) and Digital Filter (DF) method, were adapted for use in SPH simulations. Both methods could be successfully applied to the case of convected isotropic turbulence with prescribed inflow turbulence intensity as well as length- and time scale. A realistic turbulent flow field was achieved with both methods. The deviation from the prescribed turbulence intensity remained below 10 %. One of the main challenges observed is the prevention of spurious pressure waves, which may otherwise distort the turbulent flow field. Therefore, the divergence-free formulation of the RFG proved beneficial. To extend the study toward the generation of anisotropic turbulence, the RFG was applied to the turbulent flow in a pipe. The resulting Reynolds-stresses showed very good agreement with the reference DNS data, particularly near the inlet, and no significant redevelopment of turbulence was observed in the downstream direction. These findings demonstrate the capability to directly prescribe turbulent quantities at SPH boundaries, representing an important step toward extending SPH to applications involving complex turbulent flows, such as the atomization of liquid jets and sheets.

ACKNOWLEDGEMENTS

The authors acknowledge support by the state of Baden-Württemberg through bwHPC.

REFERENCES

[1] R. Vacondio et al. “Grand challenges for Smoothed Particle Hydrodynamics numerical schemes”.In: Comp. Part. Mech 8 (2021), pp. 575–588.

[2] M. Antuono et al. “Smoothed particle hydrodynamics method from a large eddy simulation perspective: Generalization to a quasi-Lagrangian model”. In: Physics of Fluids 33.1 (Jan. 2021), p. 015102. ISSN: 1070-6631.

[3] M. Okraschevski et al. “Smoothed particle hydrodynamics physically reconsidered: The relation to explicit large eddy simulation and the issue of particle duality”. In: Physics of Fluids 34.11 (Nov. 2022), p. 115108. ISSN: 1070-6631.
[4] K. Warncke et al. “Experimental and numerical investigation of the primary breakup of an air-blasted liquid sheet”. In: International Journal of Multiphase Flow 91 (2017), pp. 208–224. ISSN:0301-9322.
[5] M. Klein, A. Sadiki, and J. Janicka. “A digital filter based generation of inflow data for spatially developing direct numerical or large eddy simulations”. In: Journal of Computational Physics 186.2 (2003), pp. 652–665. ISSN: 0021-9991.
[6] S.J. Lind et al. “Incompressible smoothed particle hydrodynamics for free-surface flows: A generalised diffusion-based algorithm for stability and validations for impulsive flows and propagatingwaves”. In: Journal of Computational Physics 231.4 (2012), pp. 1499–1523. ISSN: 0021-9991.
[7] G. R. Liu and M. B. Liu. “Smoothed Particle Hydrodynamics“. WORLD SCIENTIFIC, 2003.
[8] M. Antuono, A. Colagrossi, and S. Marrone. “Numerical diffusive terms in weakly-compressible SPH schemes”. In: Computer Physics Communications 183.12 (2012), pp. 2570–2580. ISSN:0010-4655.
[9] P.N. Sun et al. “Multi-resolution Delta-plus-SPH with tensile instability control: Towards high Reynolds number flows”. In: Computer Physics Communications 224 (2018), pp. 63–80. ISSN:0010-4655.
[10] K. Szewc, J. Pozorski, and J.-P. Minier. “Analysis of the incompressibility constraint in the smoothed particle hydrodynamics method”. In: International Journal for Numerical Methods in Engineering 92.4 (2012), pp. 343–369.
[11] H. Takeda, S. M. Miyama, and M. Sekiya. “Numerical Simulation of Viscous Flow by Smoothed Particle Hydrodynamics”. In: Progress of Theoretical Physics 92.5 (Nov. 1994), pp. 939–960. ISSN: 0033-068X.
[12] M. Okraschevski et al. Evidence on the incompatibility of modern SPH methods and eddy viscosity models for scale-resolved incompressible turbulence. (2025), https://arxiv.org/abs/2506.08538.
[13] R. H. Kraichnan. “Diffusion by a Random Velocity Field”. In: The Physics of Fluids 13.1 (Jan.1970), pp. 22–31. ISSN: 0031-9171.
[14] A. Smirnov, S. Shi, and I. Celik. “Random Flow Generation Technique for Large Eddy Simulations and Particle-Dynamics Modeling”. In: Journal of Fluids Engineering 123.2 (Feb. 2001), pp. 359–371. ISSN: 0098-2202.
[15] S. Braun et al. “A framework for permeable boundary conditions in SPH: inlet, outlet, periodicity”. In: Proceedings of the 10th International SPHERIC Workshop (2015).
[16] P.N. Sun et al. “A consistent approach to particle shifting in the δ-Plus-SPH model”. In: Computer Methods in Applied Mechanics and Engineering 348 (2019), pp. 912–934. ISSN: 0045-7825.
[17] Yilei Shi et al. “Analysis of interpolation schemes for the accurate estimation of energy spectrum in Lagrangian methods”. In: Computers & Fluids 82 (2013), pp. 122–131. ISSN: 0045-7930.
[18] L. Skrbek and Steven R. Stalp. “On the decay of homogeneous isotropic turbulence”. In: Physics of Fluids 12.8 (Aug. 2000), pp. 1997–2019. ISSN: 1070-6631.
[19] Sergio Pirozzoli et al. “One-point statistics for turbulent pipe flow up to $Re_\tau \approx 6000$”. In: Journal of Fluid Mechanics 926 (2021), A28.